JOURNAL OF PROPULSION AND POWER
Vol. 40, No. 6, November–December 2024

Statistical Characterization of Emitter Fabrication over Electrospray Array Thruster

Collin B. Whittaker* and Benjamin A. Jorns†
University of Michigan, Ann Arbor, Michigan 48109

https://doi.org/10.2514/1.B39524

A method for characterizing the variance in fabrication of emitters and extractors in a porous conical electrospray array thruster is presented. Coherence scanning interferometry is used to produce topographic maps of 543 of 576 sites within the array. The emitter and extractor geometries, features of size a few hundred micrometers, are modeled as a spherically capped cone recessed from a circular aperture. Regressing this model against the topographic maps yields a set of salient parameters that describe the geometry of a site, including the tip radius and height of the emitter and its offset from the extractor aperture. Statistics over the emitter geometries are computed, which represent manufacturing tolerances. It is found that key parameters like the emitter tip radius are highly variable (mean 25.8 μm and standard deviation 20.9 μm), highlighting the stochastic nature of the manufacturing process. Correlations between the tip radius and emitter height indicate that this variability arises from blunting of the emitters during fabrication, and the observation that emitters are shorter than nominal is explained by an increase in effective cutting diameter of the tools. Further analysis indicates that determining the mean emitter tip radius of the entire population within 5% error requires over 300 individual emitter measurements. These results indicate that accurately quantifying emitter variability at scale requires rigorous and extensive analysis, and the implications of this emitter variability for device performance and design are discussed.

I. Introduction

NONUNIFORM emission presents an ongoing challenge to electrospray array thrusters. These electric microrockets consist of hundreds or thousands of individual needlelike emitter structures that produce thrust by extracting beams of charged particles from a conducting fluid via electric forces [1–5]. Experiments with small probes have demonstrated that these beams can be highly irregular across the array [6–9], and inspections after firing have shown that propellant accumulates selectively on some emitters [10]. Inhomogeneity negatively impacts device performance not only because thruster mass and area, at a premium in space, are wasted on defunct emitters but also because it increases the probability of a life-ending electrical short [11]. This problem becomes more pernicious as arrays grow greater in number, potentially limiting electrosprays to only the smallest scale propulsive applications. Characterizing sources of emission nonuniformity is thus an imperative in electrospray array thruster design and development.

A key source of variability in emission is the geometry of each emitter and its extraction electrode. The geometry influences key aspects of operation: the body of the emitter modulates fluidic transport [5,12,13], the emitter tip amplifies electric fields to induce emission [14–16], and the extractor controls the optics of the beam [17–19]. Consequently, deviations in emitter shape from nominal (i.e., manufacturing tolerances) are integral to the behavior of an array [20].

Direct characterization of emitter geometry at array scale is sparse in the literature, however. Often, assessments are limited to micrographs of a few emitters where geometries are fit by hand (e.g., superimposing a circle on the curvature of an emitter tip). Such limited inspection may not adequately represent the full population of emitters in the array. In contrast, Ma et al. [21] performed more extensive characterizations, providing the height and tip radius of up to 100 emitters. These data, however, lacked detailed analysis. Given the highly deleterious effects of emission nonuniformity stemming from inconsistent emitter geometry, more comprehensive characterization of emitter arrays is warranted.

We present here a method to systematically characterize the geometry of an electrospray array thruster, focused on systems with porous conical type emitters. The method proceeds by fitting a geometric model for the emitter-extractor system to topographic maps of the thruster produced by surface profilometry. We begin by outlining our methodology in Sec. II, describing the thruster we characterized, the nature of the topographic measurement, our model for an individual site in the array, and how we regress this model. Then, we present the results of applying these methods to the thruster in Sec. III, including an example topographic map, the best fit to the model for a single site in the array, and then statistics over the entire array. Finally, we discuss in Sec. IV how the manufacturing process may have produced the trends in geometry we observe, what implications these trends have for performance, and what improvements could be made to our methods.

II. Methodology

Our method for characterizing thruster geometry, which we detail in this section, is based on fitting a geometric model for the system to topographic maps produced by surface profilometry. First, we describe the test article characterized in this work and briefly review the use of coherence scanning interferometry to produce surface profiles. We then parameterize the geometry of a conical type electrospray emitter and extractor aperture with a model. Last, we formalize fitting this model to the training data by a least-squares analysis.

A. Test Article

For this study, we characterize the emitter geometry of the AFET-P-003, a unit in the AFET-2 family (see Ref. [2]) that we fabricated previously [22]. The emitter chip of the thruster consists of 576 square pyramidal emitters order 300 μm tall conventionally machined from a porous sintered borosilicate glass substrate (P5 grade, 1 μm pore size) using square tapered end mills. Two end mills were used to make a series of linear cuts in the substrate in serpentine patterns, one tool for each axis of the rectilinear grid of emitters. We show this tool path schematically in Fig. 1a, in which the solid circles indicate the positions of the emitters. The emitter structures are left in relief between the

Presented as Paper 2023-0260 at the 2023 AIAA SciTech Forum, National Harbor, MD, January 23–27, 2023; received 19 February 2024; accepted for publication 2 August 2024; published online 12 September 2024.

*Ph.D. Candidate, Department of Aerospace Engineering; cbwhitt@umich.edu. Student Member AIAA.

†Associate Professor, Department of Aerospace Engineering. Associate Fellow AIAA.

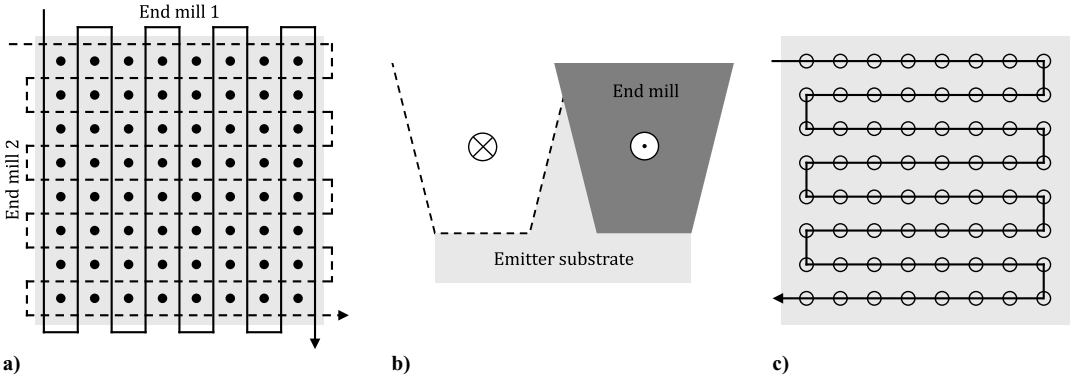

Fig. 1 Schematic of machining: a) emitter tool path, b) emitter side view, and c) extractor tool path.

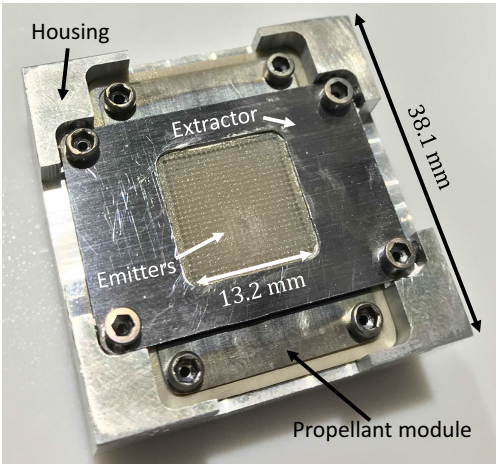

Fig. 2 Photograph of the AFET-P-003, with key dimensions labeled.

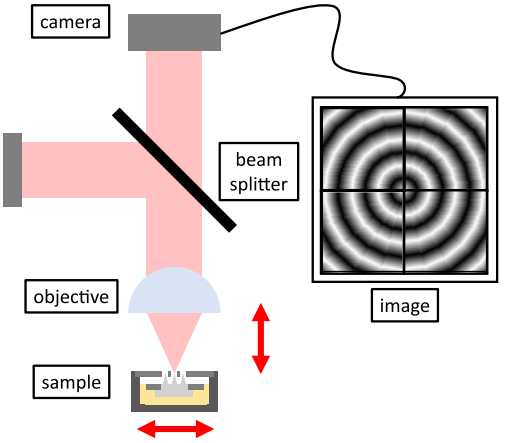

Fig. 3 Schematic of coherence scanning interferometry.

channels, with the tapered cross-section of the tools causing them to be narrower at their apex than at their base, as shown in Fig. 1b. The emitter pitch is 550 μm, and the end mills have a diameter of 380 μm at the tip with an included angle of 30 deg. The cuts were performed at a linear feed rate of 15 cm/ min and spindle speed of 30,000 rpm (the maximum of the mill), and we used a jet of compressed air pointed at the cutting tools to remove swarf.

Rather than the perforated metal sheet extractor standard on the AFET-2, the AFET-P-003 was equipped with an extractor chip consisting of a piece of MACOR ceramic metalized on one side and sitting directly against the emitter chip basal plane on the opposite side [22]. This alternative architecture is designed to provide additional structural support and resilience to shorts between the electrodes. The extractor apertures were made to be 460 μm in diameter and were machined using a miniature drill in a serpentine pattern like that of Fig. 1c. The open circles indicate positions of the extractor apertures. Finally, we give a picture of the fully assembled thruster in Fig. 2.

B. Topographic Measurement

We relied on surface profilometry to resolve the geometry of individual emitters. Profilometry produces topographic measurements of a sample; that is, it yields the height of the sample at a set of different locations. In the case of surface profilometry, the topography is resolved over a two-dimensional grid or point cloud, rendering a full three-dimensional map of the sample's surface.

For this study, we employed a Zygo Nexview NX2 system to perform coherence scanning interferometry, an advanced form of white light interferometry. As shown notionally in Fig. 3, this system channels a beam of white light to the sample through an interference objective. The beam reflected from the sample interferes with a reference beam and so produces a fringe pattern on the camera. By analyzing the change in this interference pattern as the distance of the objective from the sample is varied, the height of the sample can be determined with accuracy to order 1 nm [23]. The lateral accuracy is limited by the resolution of the camera and by the magnification of the objective, the latter also determining the measurement volume. By rastering the optics laterally, this measurement volume can be extended to capture the entirety of the sample. Such a measurement forms the basis for identifying individual emitter geometries through modeling and regression.

C. Geometry Parameterization

To facilitate quantifying emitter variability resulting from manufacturing processes, we capture the geometry of individual emitters and their extractor apertures through a set of salient parameters, that is, quantities defining the essential, macroscopic details of the system. We model the geometry as an axisymmetric, spherically capped cone recessed within a circular extractor aperture, which we depict for a single emitter and extractor aperture within an array in Fig. 4. For the AFET-P-003, the emitters are square pyramids which become rounded at the tips during manufacturing, so along the side walls of the emitter, our model will be a poorer approximation. However, this region tends not to be active in emission due to the rapid decrease in electric field strength with distance from the emitter apex, so it is more essential to capture the macroscopic side angle of the cone, which modulates fluid transport to the tip [14,24].

This representation also has the benefit of being more conducive for computational modeling (cf. Refs. [16–18]).

In this figure, (x, y, z) is a coordinate system (i.e., that of the profilometer), where z represents the height, or vertical position. The red lines in the figure divide the region containing the extractor geometry from that containing the emitter geometry. Only the top surface of the extraction electrode is exposed to the profilometer, and we model it as a horizontal plane, $z = z_a$. We take the aperture in the extractor to be a circle of radius R_a centered at $(x, y) = (x_a, y_a)$.

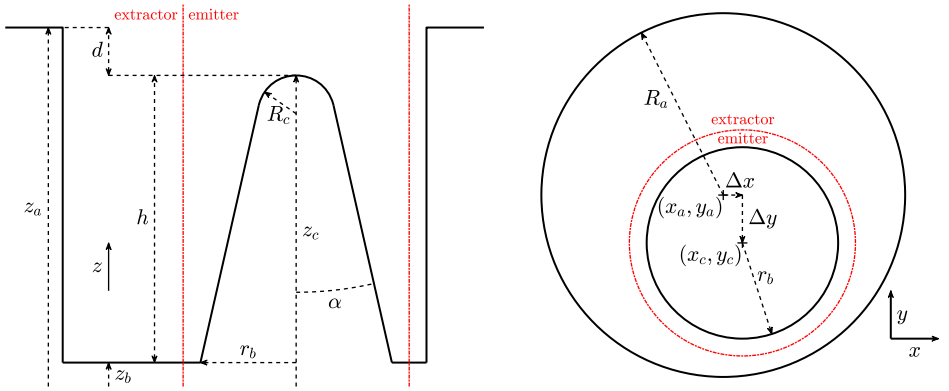

Fig. 4 Diagram showing side (left) and top (right) views of a site in the array, with coordinate conventions and key parameters of the geometric model.

The emitter structure we model as a spherically capped cone, formally, the union of a conical frustum and spherical cap, where the cap's base is coincident with the frustum's narrow base and where the frustum's conical face is tangent to the cap's spherical face. The apex of the cap is located at $(x, y, z) = (x_c, y_c, z_c)$, the radius of curvature of the cap is R_c, and the half-angle of the cone is α. The basal plane of the emitter chip is modeled as the plane $z = z_b$.

The entire geometric model is thus given compactly:

$$z = \begin{cases} z_a, & r_{\text{ex}} \geq R_a \\ z_c - R_c\left(1 - \sqrt{\left(1 - \dfrac{r_{\text{em}}^2}{R_c^2}\right)}\right), & r_{\text{em}} < R_c \cos\alpha \text{ and } r_{\text{ex}} < R_a \\ (r_b - r_{\text{em}})\cot\alpha + z_b, & r_{\text{em}} \in [R_c\cos\alpha, r_b] \text{ and } r_{\text{ex}} < R_a \\ z_b, & \text{otherwise} \end{cases} \tag{1}$$

$$r_{\text{ex}} = \sqrt{(x - x_a)^2 + (y - y_a)^2} \tag{2}$$

$$r_{\text{em}} = \sqrt{(x - x_c)^2 + (y - y_c)^2} \tag{3}$$

$$r_b = [z_c - z_b - R_c(1 - \sin\alpha)]\tan\alpha + R_c\cos\alpha \tag{4}$$

Here, r_{ex} is the lateral distance of a point (x, y) from the center of the aperture, r_{em} is instead the distance from the center of the emitter, and r_b is the basal radius of the emitter.

With these, we have fully described the site geometry by a set of parameters we can regress against the profilometry measurements. It is further useful, however, to define a set of reduced parameters that describe the relative geometry of the system rather than its absolute position within a coordinate system,

$$h = z_c - z_b \tag{5a}$$

$$d = z_a - z_c \tag{5b}$$

$$\Delta x = x_c - x_a \tag{5c}$$

$$\Delta y = y_c - y_a \tag{5d}$$

$$t_e = z_c - z_b \tag{5e}$$

with h being the height of the emitter, d being the distance the emitter is recessed from the extractor, and Δx and Δy being the lateral misalignments between the aperture and emitter in x and y, respectively. The quantity t_e is the thickness of the extractor, which for the AFET-P-003 sits directly against the emitter basal plane.

D. Model Regression

To reduce the raw topographic point data returned from the surface profilometry into salient device dimensions, we adopt a least-squares model regression framework. In our case, given a set of N data $\{(z; x, y)_j\}$ and a model of the form $z = F(x, y; \theta)$, where $j = 1, 2, \ldots, N$ and θ is the set of model parameters, the least-squares fit is the set of parameter values $\hat{\theta}$ satisfying

$$\hat{\theta} = \underset{\theta}{\text{argmin}} \sum_{j=1}^{N} \Big(F(x_j, y_j; \theta) - z_j\Big)^2 \tag{6}$$

While in principle we could fit our model to both the emitter and extractor geometry simultaneously, because these features are present in separate regions of the domain, the parameters defining the emitter are nearly independent from those defining the extractor. Hence, it is more efficient to subdivide the domain between these two regions (see Fig. 4) and regress corresponding subsets of parameters independently from the subdivided data,

$$\hat{\theta}_{\text{em}} = \underset{\theta_{\text{em}}}{\text{argmin}} \sum_{(x_j, y_j) \in \Omega_{\text{em}}} \Big(F(x_j, y_j; \theta_{\text{em}}) - z_j\Big)^2 \tag{7}$$

$$\hat{\theta}_{\text{ex}} = \underset{\theta_{\text{ex}}}{\text{argmin}} \sum_{(x_j, y_j) \in \Omega_{\text{ex}}} \Big(F(x_j, y_j; \theta_{\text{ex}}) - z_j\Big)^2 \tag{8}$$

where Ω_{em} denotes the emitter subdomain and Ω_{ex} the extractor subdomain. θ_{em} is the subset of parameters of Eq. (1) that defines the emitter geometry, $\theta_{\text{em}} = (z_b, x_c, y_c, z_c, R_c, \alpha)$, and θ_{ex} is the subset defining the extractor geometry, $\theta_{\text{ex}} = (z_b, x_a, y_a, R_a, z_a)$. Dividing the domain in this way produces two separate estimates to z_b. For all computations in this study [e.g., Eq. (5a)], we use the estimate from the emitter domain, as it is more physically meaningful.

We have thus identified a methodology to determine individual emitter geometries for an electrospray array. By regressing a simplified model for the geometry against surface profilometry data, we obtain the best fit of the parameters to the model for each site in the array. We determine the site geometries of the AFET-P-003 using this procedure in Sec. III.

III. Results

In this section, we describe the results of applying the methodologies of Sec. II to characterize the geometry of a porous conical electrospray array thruster. We open the section by describing the profilometry taken of the thruster and presenting an example topographic map. We follow by comparing the best-fit model prediction for a single site in the array against the raw data. We end by computing statistics over the entire population of sites we characterized.

A. Thruster Profilometry

We mapped the emission region of the thruster (a volume approximately $13.2 \times 13.2 \times 0.5$ mm) via coherence scanning interferometry (cf. Sec. II.B). The lateral resolution (i.e., pixel size) was 350 nm. As a result of this fine resolution and the limited computer memory available to the profilometer, we divided the 24×24 emitter grid into nine 8×8 subregions, which we denote by cardinal directions (northwest, north, northeast, etc.). One subregion, the northwest (NW), was limited to only a 6×6 grid, and a further five emitters were occluded by particulates such as lint and were not well suited to analysis. In total, then, we were able to capture 543 of 576 emitters in the array; we number all 576 sites sequentially in row-major order for reference.

We show an example topographic map, that of the southwest (SW) region, in Fig. 5. The map illustrates several high-level details of the thruster's fabrication. First, the emitters are square pyramidal structures recessed from the extractor and situated approximately centered within their respective apertures. Second, emitter geometry is nonuniform, most evident by the variance in emitter height across the array. Indeed, we find that a small proportion (less than 2%) of emitters were removed from the chip almost entirely, having been uprooted from the substrate during machining (e.g., numbers 385 and 553 in Fig. 5). Figure 5 also shows that, while some emitters are sharply tipped, others have blunt apexes. Finally, we observe that the emitter chip basal plane is punctuated by linear ridges in the x direction, rather than being flat as expected (the substrate porosity notwithstanding). Because separate cutting tools were used for x-aligned and y-aligned cuts, this feature likely resulted from an error in setting the machining depths of one of the tools, a point we expand upon in the discussion.

B. Geometry Regression

After capturing surface profiles of the different regions, we computed best fits of our geometry model (see Sec. II.D) to each of the 543 sites we were able to capture. We procedurally segmented the topographic data into individual sites, and thereafter emitter and extractor subdomains, through a user-assisted preprocessing program. The model (1) is discontinuous and nonlinear in its parameters, precluding an exact solution to Eqs. (7) and (8). We therefore approximate the best-fit parameters through numerical minimization, in our case, a Nelder–Mead method (see also Ref. [25]).

Figure 6 summarizes the results of this regression for a single site in the array, site 097 in the NW region. This site is closest to having the

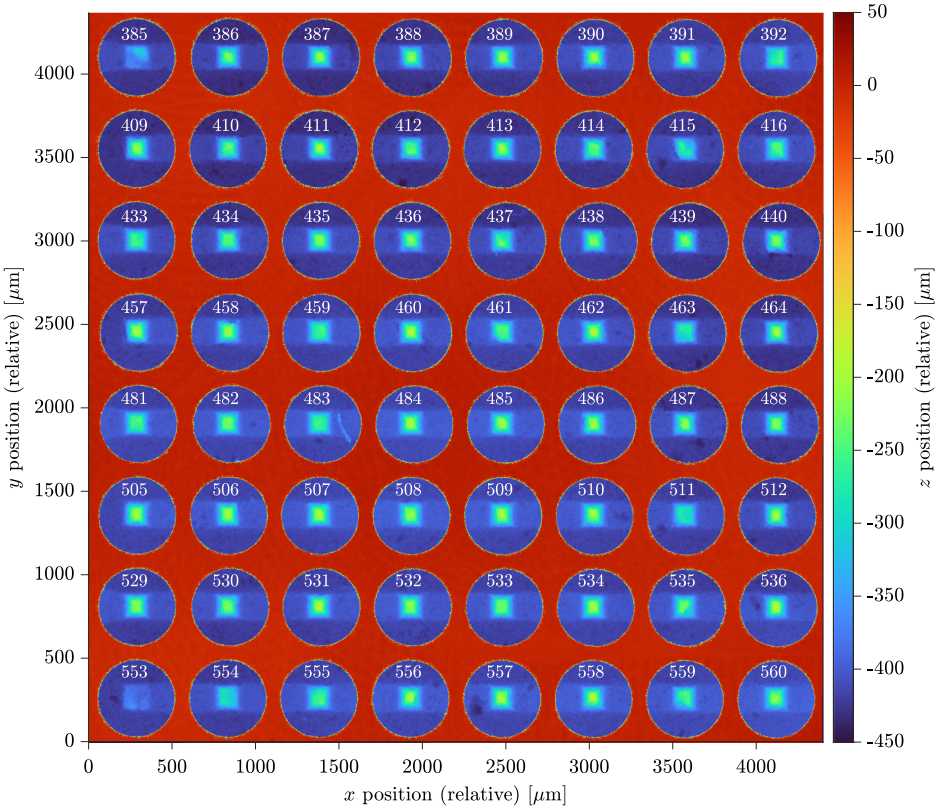

Fig. 5 Topographic map of the SW subregion of the thruster.

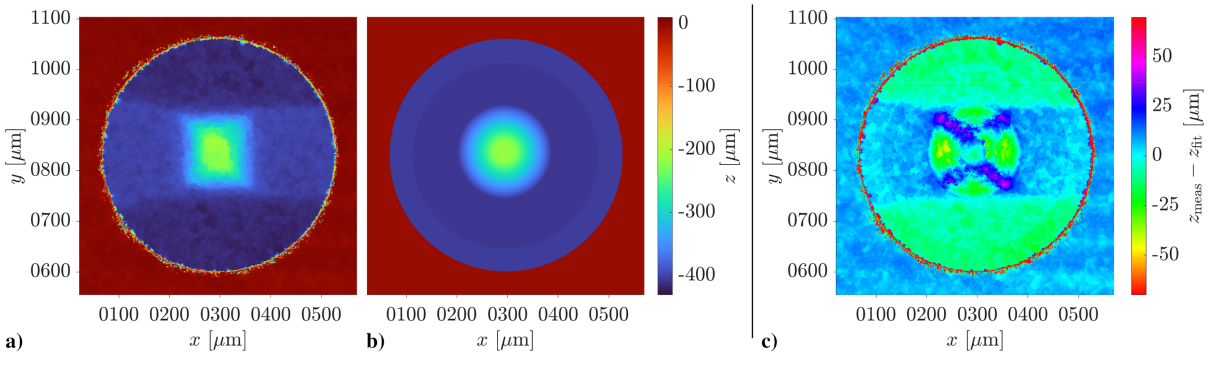

Fig. 6 Heat maps for site 097: a) the measured data, b) the least-squares model fit, and c) the residual between the two.

mean geometry among all emitters (cf. Sec. III.C). The left two heat maps are colored on the same scale and show the measured data over the entire site next to the best fit to the geometric model. The rightmost heat map shows the residual $z_{\text{meas}} - z_{\text{fit}}$ on a different color scale. Further, in Table 1, we provide the best-fit parameters over the emitter and extractor domains alongside the parameters of Eqs. (5) computed therefrom. We also include the emitter base radius r_b [see Eq. (4)].

Table 1 Best-fit parameters for site 097; left to right: emitter domain parameters, extractor domain parameters, and derived quantities

Emitter	Value	Extractor	Value	Relative	Value
z_c	−215.2 μm	z_a	−5.6 μm	d	209.6 μm
z_b	−407.5 μm	z_b	−404.4 μm	h	192.3 μm
x_c	294.2 μm	x_a	297.3 μm	Δx	−3.1 μm
y_c	837.5 μm	y_a	830.9 μm	Δy	6.6 μm
R_c	27.3 μm	R_a	230.0 μm	r_b	93.2 μm
α	0.370 rad	— —	— —	t_e	401.9 μm

Table 2 Summary statistics of sites in the electrospray array

Parameter	Mean	Median	Standard deviation
R_c, μm	25.8	20.9	18.6
h, μm	192.5	202.8	36.0
α, rad	0.364	0.352	0.053
d, μm	204.2	195.1	38.1
R_a, μm	230.0	230.0	0.4
Δx, μm	−7.8	−7.7	11.1
Δy, μm	7.3	8.0	8.5
t_e, μm	396.7	399.4	11.7
r_b, μm	89.7	89.5	4.5

Figure 6 and Table 1 illustrate several common features of sites in the array. We observe in the residual heat map (Fig. 6c) that the best fit (part b) agrees with the measurement (part a) within 10 μm over the majority of the domain, particularly at the surface of the extractor, the emitter basal plane, and the apex of the emitter. Figure 6 also demonstrates that the least-squares fit to z_b lies in between the top and bottom surface of the x-aligned ridges we first observed in Fig. 5, and Table 1 indicates that the values of z_b for the emitter and extractor subdomains disagree, though only by a few micrometers.The residual tends to be larger (20 − 50 μm) on the body of the emitter, forming a distinctive X pattern. This is a result of our simplifying the emitter body as perfectly conical in the model, when the emitters are square pyramids (cf. Sec. II.C). The best-fit cone is a compromise between the faces and corners of the emitter body (i.e., the base of the cone is between the incircle and circumcircle of the square base). Finally, we see that disagreement is largest at the edge of the extractor aperture, which results because of the large discontinuity in height and the small but resolvable roughness in the aperture.

C. Manufacturing Statistics

Having computed the best approximation of the model to each site we measured, we now examine the statistics of the entire population of sites, which provide insight into the quality and reliability of their manufacture. We collect in Table 2 summary statistics of the parameters $\theta = (R_c, h, \alpha, d, R_a, \Delta x, \Delta y)$ taken over all sites. The set θ fully defines the geometry model, but as additional reference, we include statistics for the extractor thickness t_e and the emitter base radius r_b. In addition to these summary statistics, we present a corner plot of θ for the entire population in Fig. 7. This matrix of plots is modeled on a covariance matrix: the diagonal figures are histograms for each parameter over all 543 sites, while the off-diagonal figures are scatter plots of the sites for each pair of parameters. This serves to highlight the distribution and correlation between parameters.

Our qualitative observation of variability in emitter geometry made in light of Fig. 5 is confirmed here quantitatively by the analysis. As

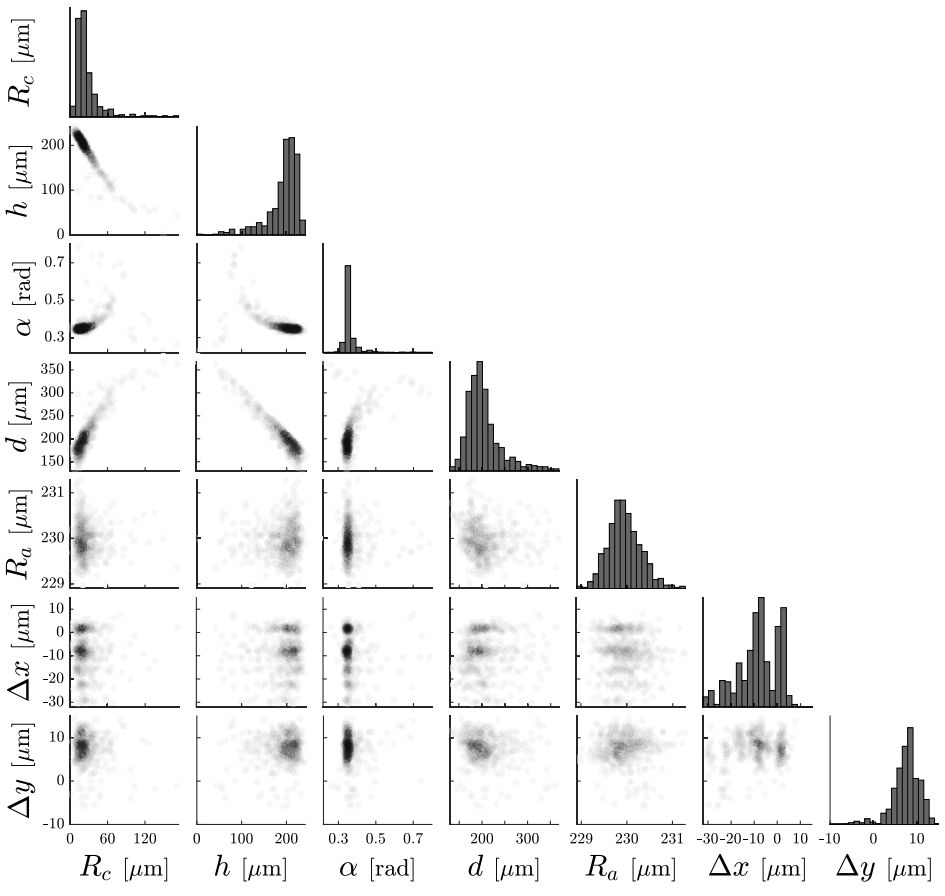

Fig. 7 Corner plot highlighting distribution in site geometry.

Fig. 7 and Table 2 both show, the tip radius of curvature R_c, emitter height h, and recession d all vary substantially, with standard deviations large on the order of the measurement (greater than 15 μm). This suggests that these features were not reliably produced in manufacturing the array. The tails of the distributions in Fig. 7 correspond to partially or wholly broken emitters, most evident from their small height h. In contrast, the cone angle α and aperture radius R_a are narrowly distributed, suggesting they are well controlled during fabrication. This makes sense because both of these are enforced automatically by the geometry of the tool: the taper of the end mill used to machine the emitters in the case of α and the diameter of the drill used to bore the extractor apertures for R_a. Additionally, the misalignment parameters Δx and Δy have nonzero means, suggesting there is a bulk offset between the extractor and emitter chips of order 10 μm. While Δy is unimodally distributed about its mean, Fig. 7 indicates that Δx is multimodal, suggesting distinct subpopulations of sites are present.

We also observe that the parameters R_c, h, and d are highly correlated, that they do not vary independently of each other. This manifests as the sharp lines in Fig. 7, in contrast to the sparser clouds characteristic of parameters like R_a. The correlation between h and d is explained by the fact that the thickness of the extractor chip t_e does not vary strongly over the area of the chip in comparison to h (cf. Table 2). Because the extractor in this design sits directly on top of the emitter chip, the top of the extractor is thus nearly a fixed distance removed from the basal plane of the emitters, and so a shorter emitter is necessarily recessed deeper. That is, for some constant c, we have that $z_a - z_b = h + d \approx c$, and hence $h \propto -d$. We draw a similar conclusion for the correlation between R_c and h by noting that Table 2 indicates the emitter base radius is also nearly constant. Combined with the well-controlled side wall angle α, this fixed base width implies that if an emitter is shorter (smaller h) its apex must necessarily be broader (larger R_c). Hence, as additional material is removed from the emitter tip as a result of nonidealities in the manufacturing process, the emitter becomes more blunt as a result. Mathematically, noting $h = z_c - z_b$ and rearranging Eq. (4) yields

$$h = r_b \cot\alpha - R_c(\cos\alpha \cot\alpha + \sin\alpha - 1) \tag{9}$$

which reduces to the proportionality $h \propto -R_c$ assuming α and r_b are constant.

We now determine if this variability in geometry arises out of any systematic variation across the array, for example, if emitters tend to be shorter on one side than the opposite. In Figs. 8 and 9, we plot, respectively, R_c and Δx for each site in the array, arranged as scatter plots in the shape of the grid of sites. The markers with inscribed question marks represent the sites we did not characterize. We observe that for the emitter tip radius there is no strong dependence on position in the array, with sites of sharper or duller emitters scattered across the thruster. This strongly suggests that its variation arises out of a stochastic process during machining and not from more systematic sources (e.g., tool wear). In contrast, Δx takes a largely consistent value across each row but varies discretely from row to row. This accounts for the multiple peaks visible in Fig. 7. We note the apertures in the extractor were machined in just such a serpentine pattern, suggesting that the discrepancy between rows emerged as a result of backlash in the milling machine, that is, positional error caused by a reversal in the lateral motion of the tool. This interpretation is supported by Fig. 5, in which an alternating offset in the aperture positions is visible.

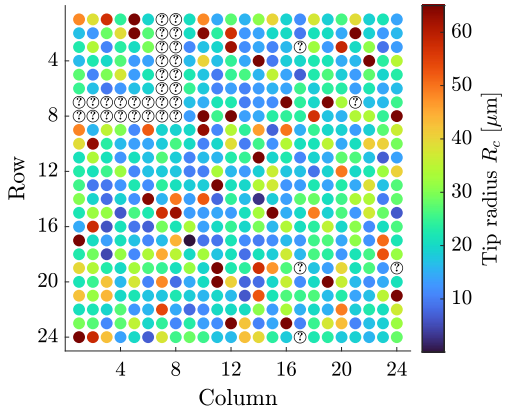

Fig. 8 Scatter plot of emitter tip radius R_c over the electrospray array.

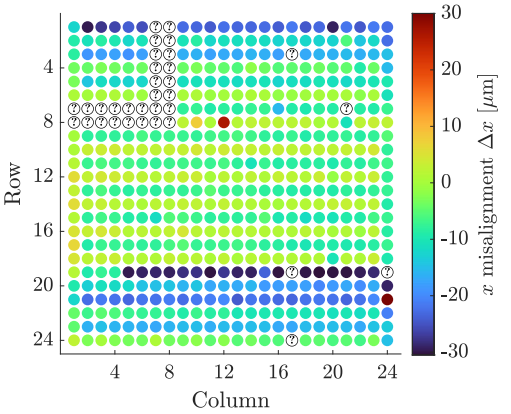

Fig. 9 Scatter plot of x misalignment Δx over the electrospray array.

In summary, we have determined the geometry for 543 of 576 sites within an electrospray array thruster. We found that, while some parameters tend to be well controlled during the machining process (namely, R_a and α), the remaining parameters vary more greatly across the array and are often highly correlated. These data have key implications for the manufacturing process and for further analyses of array performance, which we consider in Sec. IV.

IV. Discussion

In this section, we discuss our results. We first analyze their implications for the manufacturing process; we then outline their use in treating array performance probabilistically in modeling and experiment. Finally, we describe possible refinements to our methods.

A. Manufacturing Process

The results of Sec. III constitute an extensive characterization of the AFET-P-003's fabrication, analyzing 543 of 576 sites within the array. These data encode the tolerances in the manufacturing process, that is, how accurately and repeatably it can produce a given design. We observed that, while the aperture radius, cone half-angle, and base radius (R_a, α, and r_b) were reliably controlled during manufacture, the emitter tip radius, emitter height, and recession (R_c, h, and d) were highly variable and correlated to each other, the result of emitter blunting during the cutting operation. We also determined that this blunting occurs incoherently across the array, suggesting this mechanism arises stochastically.

This analysis facilitates identifying how different fabrication parameters map to changes in system geometry. As an illustrative example, we contrast our results for the AFET-P-003 to the realization of the AFET-2 system introduced by Natisin et al. [2]. In that study, the authors indicate loosely that their emitters have tip radii between 10 to 20 μm, which, given the target emitter height of 300 μm, maps to a height about 275 to 250 μm after accounting for blunting of the emitters per Eq. (9). With reference to Table 2, we note that the AFET-P-003 has emitters with substantially smaller height (by 80 μm) and greater radius of curvature (by $5 - 10$ μm). Consistent with our analysis in Sec. III.C, the discrepancy in height is partially the result of the larger radii of curvature characterized here. This may be caused by a difference in machining parameters, in particular the spindle speed of the bit, which Ref. [2] suggests played a key role in ensuring sharp emitters. While the authors of Ref. [2] ran their cutting operation at 50,000 rpm, the machine used to make the AFET-P-003 was limited to only 30,000 rpm, potentially exacerbating the nonideality that causes fractures of the emitter tips.

This alone, however, is not sufficient to explain the difference in height of the emitters. A median emitter tip radius of 20 μm matches to 250 μm height, which is 50 μm more than our median height of 200 μm. On further inspection, the remaining discrepancy is explained by a systematic overcutting of the emitters, the removal of more material from the substrate than targeted nominally. Using our median value for the cone half-angle in Table 2, we compute the expected basal radius of the emitters of Ref. [2] to be 110 μm, within our approximation of the pyramidal structure by a cone. This is substantially larger than the 90 μm radius found for the AFET-P-003. When we substitute our smaller base radius back into Eq. (9), the same 10 to 20 μm tip radius results instead in heights from 225 to 200 μm, precisely in line with those found here. While we expect that the offset error that produced the linear ridges contributes to this overcutting, making deeper cuts along the x axis, this should only reduce their height by the height of the ridge, about 20 μm. We thus conclude the emitters must also have been overcut laterally; that is, as a result of the tool having a larger diameter or there being additional runout (i.e., precession) in the spindle, the channels between emitters were cut wider than nominal, narrowing and shortening the emitters as a consequence. This kind of variability from tool to tool may be minimized by first *proving* them to experimentally characterize their cutting width and adjusting machining paths to compensate.

These analyses of the manufacturing process form the foundation of constructing a formal parametric model which maps changes in machining parameters to changes in device geometry. With sufficient validation, the model would predict the machining parameters necessary to achieve a desired geometry, and how reliably it might be produced. This work indicates that fully quantifying the variability of emitters at scale requires comprehensive treatment. To illustrate this point, we simulate the results of characterizing smaller sample sizes, N_s, of sites in Fig. 10. For each value of N_s, we draw a combination of N_s unique sites from those measured and compute their mean emitter tip radius, then repeat this process 10^5 times. The shaded region between the dashed lines contains 95% of these subsamples, representing the range of mean values for R_c we could have found if we had measured fewer emitters. We observe that for small sample sizes ($N_s < 10$) the estimate to R_c is essentially unreliable, potentially off by a factor 1.5. Indeed, a sample size of 50 is required to estimate the true sample mean of 25.8 μm within $\pm$20%, 300 is required to be within 5%, and 500 is required to be within 1%. Thus, a robust characterization of tip radius (key to discriminating between choices of manufacturing parameters or feeding into an emission model) requires characterizing a large population of emitters, at least for the AFET-P-003. For geometric parameters well controlled during fabrication (e.g., R_a and α), a simple point inspection of a few sites is likely sufficient to serve as validation, however. For comparison, we plot in Fig. 10 the same analysis performed for the aperture radius (dash-dotted lines), where we have scaled the axes to be the same width relative to their respective sample means. We find here that even a single sample of R_a is sufficient to reliably estimate the true sample mean of 230.0 μm within 1% error. Altogether, then, adequately quantifying emitter variability and assessing the effects of manufacturing processes requires rigorous analysis to understand the statistical properties of sites within an array.

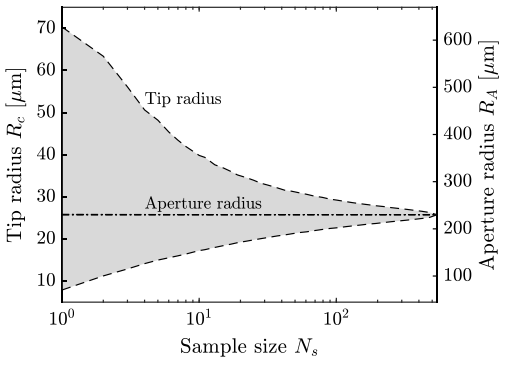

Fig. 10 Convergence of sample mean for tip radius and aperture radius as a function of sample size.

B. Implications for Array Performance

Rigorously capturing emitter geometry variability in detail is crucial for accurately capturing device performance. Evidence of emission nonuniformity in thrusters is commonly reported in previous work [6–10], and variations in geometry (particularly in the sharpness of the emitter tip) have been shown to greatly influence device operation [26–28]. Indeed, the scatter plot for R_c of Fig. 8 is qualitatively similar to, for example, the spatially resolved beam current maps of Ref. [6]. Nonuniformity stemming from emitter variability is particularly hazardous to device lifetime because it can contribute to shorts between the extractor and emitter [11].

Predicting the consequences of inhomogeneous emitter geometry via modeling is key to designing against these failure modes. In previous work, we demonstrated that accounting for irregular geometry was necessary to capture the inflected current-voltage characteristic of an AFET-2 thruster [20], a consequence of emitters activating at different voltages. In performing these computations, however, we made major assumptions about the emitter geometries, in particular considering the different geometric parameters as being independently distributed. In light of the present study, our prior assumptions in Ref. [20] likely underestimated emission nonuniformity in the array by ignoring correlation between parameters. For example, greater recession d and larger tip radius R_c both correspond to weaker electric fields that discourage emission, and these parameters were highly correlated for our system. Furthermore, because the geometry of any individual emitter in the array was unknown, it was necessary in Ref. [20] to sample over many possible realizations of each emitter to account for this uncertainty. This enhanced the computational expense of the model and contributed additional uncertainty to predictions; these detrimental effects would be mostly eliminated if information like that gathered here were available.

Predictively modeling emission irregularities is greatly supplemented by experimental validation data, with the most elementary in electrospray propulsion being the current-voltage characteristic of a thruster. As previously discussed, the blunt emitter geometries of the AFET-P-003 should result in lower emission current as a function of voltage. Indeed, in previous experiments with the AFET-P-003 [22], we observed exactly this, demonstrating a maximum steady-state emission current of 50 μA, whereas the AFET-2 of Ref. [2] was able to source over 700 μA. We found that these disparate yields could be reconciled if the electric field strength of the AFET-P-003 was a factor 2.2 lower on average. Performing electrostatic simulations of emitter geometry, we find that the mean emitter parameters of Table 2 result in an electric field approximately a factor 1.9 times weaker than a *mean* emitter reconstructed from information in Ref. [2]. While this single point comparison is not fully representative of the entire emitter population, it does indicate that duller emitters are the key driver of the lower emission yield.

C. Method Improvements

Altogether, the present method of emitter characterization represents a potent tool for electrospray array development. By adopting a geometric model for emitter geometry, we provide a set of quantitative parameters to inform manufacturing, modeling, and experimentation. Furthermore, the formalism of the model allows these parameters to be computed procedurally at scale and without human judgment, providing rigor and repeatability. This capability is supported by using surface profilometry to resolve features at a level beyond visual inspection.

The method is not without its limitations, however. First, each of the nine different subregions of the thruster took 12 h to image on the profilometer, for a total of 108 h of machine time. This imaging time is driven heavily by the lateral resolution in the measurement, as the profilometer must stitch together many different images as it rasters across the measurement region. We chose the lateral resolution of 350 nm in this work to be arbitrarily precise for the large-scale emitter features we wanted to resolve. It is likely the case that this can be

reduced while still capturing the emitter geometry, with large benefit: a factor 2 decrease in resolution (to 700 nm pixel size) corresponds to four times faster imaging. Relatedly, the AFET-P-003 was still filled with propellant from testing when we imaged it, making the substrate more translucent and reducing signal to the profilometer. This necessitated longer exposure times during imaging; such overhead can be reduced by mapping the thruster when it is dry and it scatters light more effectively. Together, these modifications would allow an entire thruster to be characterized within a day.

Second, we have not treated the uncertainty in the best-fit parameters produced by our algorithm. That is, there may be multiple sets of parameters θ that represent a good fit to the data. This arises from our macroscopic approximation to the detailed microscopic features of the emitter (e.g., surface roughness) and the finite resolution of the measurement. For our purposes, we were concerned primarily with trends among the population of emitters rather than the detailed geometry of any single emitter. However, for applications like model validation on single emitter tests, a robust understanding of uncertainty in the emitter geometry is warranted in making inferences about the model, as could be interrogated with a more formal statistical framework (e.g., Bayesian inference).

V. Conclusions

This study has explored a method for characterizing individual electrospray emitter geometries at array scale. The foundation of this method is using surface profilometry, in this case coherence scanning interferometry, to produce a topographic map of the thruster. Focusing the analysis on porous conical electrosprays, the authors modeled each site within an array as a spherically capped cone recessed within a circular aperture. This geometric model incorporates several parameters like the emitter tip radius and height that describe the emitters and extractor apertures at a high level. Least-squares regression of the model against data from the surface profilometry can thus be used to determine the geometry of each of the emitters.

The authors applied this analysis to the AFET-P-003, a porous conical type electrospray array thruster in the AFET-2 family that uses an alternative extractor architecture consisting of a metalized ceramic resting directly against the emitter chip. They found that the model was able to approximate emitter geometries within 10 μm over most of the domain. The biggest discrepancies resulted from setup errors in the machining process and from approximating the square pyramidal emitters as a cone. When computing statistics over the best-fit parameters to each site, the authors determined that the aperture radius, cone half-angle, and emitter base radius (R_a, α, and r_b) are well controlled during the machining operation, within ± 0.4 μm, ± 3 deg, and ± 4.5 μm respectively. In contrast, they observed that the emitter tip radius, emitter height, and recession (R_c, h, and d) were highly variable across the array (± 18.6 μm, ± 36.0 μm, and ± 38.1 μm respectively) and were correlated to each other. They concluded the correlation between these parameters arises because the base radius and angle of the cone body are nearly fixed, necessitating that when excess material is removed from the machining operation it both dulls the tip and shortens the emitter. They also discovered that this blunting of emitters was scattered incoherently across the array, suggesting it arises largely randomly and not as a result of a systematic process like tool wear.

When the authors compared their results to data published previously for an AFET-2 system, they surmised that a bulk discrepancy in emitter height between the two systems resulted from their cutting tool being oversize or having larger than expected runout. Correspondingly, they suggested proving emitter chip cutting tools as an avenue to improve manufacturing repeatability. They also found that, independent of this height discrepancy, their emitters were duller, having $5 - 10$ μm larger R_c on average. They postulated this was the result of the lower spindle speed used to cut the emitter structures, as spindle speed has been cited previously as a key to achieving sharp emitter structures when conventionally machining. Further, when they simulated the effect of measuring fewer sites within the array, they determined that a sample size of 300 emitters was necessary to compute the true sample mean of 25.8 μm within 5%, suggesting extensive emitter characterization can be required to accurately assess variability.

In total, the method presented here has great utility as a tool to support further analysis. By providing extensive quantitative data by which to evaluate the fabrication of porous conical electrosprays, the authors support parametrically investigating machining processes to ensure quality and repeatability. Additionally, understanding the geometry of individual emitters in an array (and the distribution in those geometries) is a potent validation point when performing predictive modeling or interpreting experimental results. This is because nonuniformity in device geometry invites nonuniformity in current emission when the thruster is operated, which has negative consequences for system performance and lifetime. Detailed emitter geometry characterization is a key tool in the design and development of robust and resilient electrospray thruster architectures.

VI. Data Availability Statement

The data used in this study and the computer codes used to analyze them have been made available in an external repository [25].

Acknowledgments

This work was supported by a NASA Space Technology Graduate Research Opportunity (grant number 80NSSC21K1247). This research was supported in part through computational resources and services provided by Advanced Research Computing, a division of Information and Technology Services at the University of Michigan, Ann Arbor. The authors would like to thank Jon Mackey and other staff of NASA John H. Glenn Research Center at Lewis Field for their help in learning to operate the profilometer. Collin B. Whittaker would also like to thank Thomas Liu of NASA John H. Glenn Research Center at Lewis Field for his continued mentorship.

References

[1] Lozano, P. C., Wardle, B. L., Moloney, P., and Rawal, S., "Nanoengineered Thrusters for the Next Giant Leap in Space Exploration," *Materials Research Society Bulletin*, Vol. 40, No. 10, 2015, pp. 842–849. https://doi.org/10.1557/mrs.2015.226

[2] Natisin, M. R., Zamora, H. L., McGehee, W. A., Arnold, N. I., Holley, Z. A., Holmes, M. R., and Eckhardt, D., "Fabrication and Characterization of a Fully Conventionally Machined High-Performance Porous-Media Electrospray Thruster," *Journal of Micromechanics and Microengineering*, Vol. 30, No. 11, 2020, Paper 115021. https://doi.org/10.1088/1361-6439/abb8c3

[3] Legge, R. S., and Lozano, P. C., "Electrospray Propulsion Based on Emitters Microfabricated in Porous Metals," *Journal of Propulsion and Power*, Vol. 27, No. 2, 2011, pp. 485–495. https://doi.org/10.2514/1.50037

[4] Krejci, D., Mier-Hicks, F., Fucetola, C., Lozano, P., Schouten, A. H., and Martel, F., "Design and Characterization of a Scalable Ion Electrospray Propulsion System," *34th International Electric Propulsion Conference*, Electric Rocket Propulsion Soc., July 2015, p. 149, https://www.electricrocket.org/index.php?page=iepc-article-repository.

[5] Cisquella-Serra, A., Galobardes-Esteban, M., and Gamero-Castaño, M., "Scalable Microfabrication of Multi-Emitter Arrays in Silicon for a Compact Microfluidic Electrospray Propulsion System," *American Chemical Society Applied Materials & Interfaces*, Vol. 14, No. 38, 2022, pp. 43,527–43,537. https://doi.org/10.1021/acsami.2c12716

[6] Guerra-Garcia, C., Krejci, D., and Lozano, P., "Spatial Uniformity of the Current Emitted by an Array of Passively Fed Electrospray Porous Emitters," *Journal of Physics D: Applied Physics*, Vol. 49, No. 11, 2016, Paper 115503. https://doi.org/10.1088/0022-3727/49/11/115503

[7] Courtney, D. G., Wood, Z., and Fedkiw, T., "Reconstructing Electrospray Plume Current Spatial Distributions Using Computed Tomography," *36th International Electric Propulsion Conference*, Electric Rocket Propulsion Soc., Sept. 2019, p. 787, https://www.electricrocket.org/index.php?page=iepc-article-repository.

[8] Fedkiw, T. P., Wood, Z. D., and Demmons, N., "Improved Computed Tomography Current Mapping of Electrospray Thrusters," *AIAA Propulsion and Energy 2021 Forum*, AIAA Paper 2021-3389, July 2011. https://doi.org/10.2514/6.2021-3389

[9] Wright, P. L., Uchizono, N. M., Collins, A. L., and Wirz, R. E., "Characterization of a Porous Tungsten Electrospray Emitter," *37th International Electric Propulsion Conference*, Electric Rocket Propulsion Soc., June 2022, p. 232, https://www.electricrocket.org/index.php?page=iepc-article-repository.

[10] Krejci, D., Mier-Hicks, F., Thomas, R., Haag, T., and Lozano, P., "Emission Characteristics of Passively Fed Electrospray Microthrusters with Propellant Reservoirs," *Journal of Spacecraft and Rockets*, Vol. 45, No. 2, 2017, pp. 447–458. https://doi.org/10.2514/1.A33531

[11] Jorns, B. A., Gorodetsky, A., Lasky, I., Kimber, A., Dahl, P., St. Peter, B., and Dressler, R., "Uncertainty Quantification of Electrospray Thruster Array Lifetime," *36th International Electric Propulsion Conference,*, Electric Rocket Propulsion Soc., Sept. 2019, p. 317.

[12] Courtney, D. G., and Shea, H., "Influences of Porous Reservoir Laplace Pressure on Emissions from Passively Fed Ionic Liquid Electrospray Sources," *Applied Physics Letters*, Vol. 107, No. 10, 2015, Paper 103504. https://doi.org/10.1063/1.4930231

[13] Coffman, C. S., Martínez-Sánchez, M., and Lozano, P. C., "Electrohydrodynamics of an Ionic Liquid Meniscus During Evaporation of Ions in a Regime of High Electric Field," *Physical Review E*, Vol. 99, No. 6, 2019, Paper 063108. https://doi.org/10.1103/PhysRevE.99.063108

[14] Coffman, C., Martinez-Sanchez, M., Higuera, F., and Lozano, P. C., "Structure of the Menisci of Leaky Dielectric Liquids During Electrically-Assisted Evaporation of Ions," *Applied Physics Letters*, Vol. 109, No. 23, 2016, Paper 231602. https://doi.org/10.1063/1.4971778

[15] Gallud, X., and Lozano, P. C., "The Emission Properties, Structure and Stability of Ionic Liquid Menisci Undergoing Electrically Assisted Ion Evaporation," *Journal of Fluid Mechanics*, Vol. 933, Feb. 2022, Paper A43. https://doi.org/10.1017/jfm.2021.988

[16] Whittaker, C. B., and Jorns, B. A., "Modeling Multi-Site Emission in Porous Electrosprays Resulting from Variable Electric Field and Meniscus Size," *Journal of Applied Physics*, Vol. 134, No. 8, 2023, Paper 083301. https://doi.org/10.1063/5.0159396

[17] Petro, E. M., Gallud, X., Hampl, S. K., Schroeder, M., Geiger, C., and Lozano, P. C., "Multiscale Modeling of Electrospray Ion Emission," *Journal of Applied Physics*, Vol. 131, No. 1, 2022, Paper 193301. https://doi.org/10.1063/5.0065615

[18] Asher, J., Huang, Z., Cui, C., and Wang, J., "Multi-Scale Modeling of Ionic Electrospray Emission," *Journal of Applied Physics*, Vol. 131, No. 1, 2022, Paper 014902. https://doi.org/10.1063/5.0071483

[19] Gamero-Castaño, M., and Galobardes-Esteban, M., "Electrospray Propulsion: Modeling of the Beams of Droplets and Ions of Highly Conducting Propellants," *Journal of Applied Physics*, Vol. 131, No. 1, 2022, Paper 013307. https://doi.org/10.1063/5.0073380

[20] Whittaker, C. B., Gorodetsky, A. A., and Jorns, B. A., "Model Inference from Electrospray Thruster Array Tests," *AIAA SciTech 2022 Forum*, AIAA Paper 2022-0041, Jan. 2022. https://doi.org/10.2514/6.2022-0041

[21] Ma, C., Bull, T., and Ryan, C. N., "Plume Composition Measurements of a High-Emission Density Electrospray Thruster," *Journal of Propulsion and Power*, Vol. 37, No. 6, 2021, pp. 816–831. https://doi.org/10.2514/1.B37996

[22] Whittaker, C. B., and Jorns, B. A., "A Self-Healing Extractor for Electrospray Arrays," *37th International Electric Propulsion Conference*, Electric Rocket Propulsion Soc., June 2022, p. 206, https://www.electricrocket.org/index.php?page=iepc-article-repository.

[23] de Groot, P., "Principles of Interference Microscopy for the Measurement of Surface Topography," *Advances in Optics and Photonics*, Vol. 7, No. 1, 2015, pp. 1–65. https://doi.org/10.1364/AOP.7.000001

[24] Courtney, D. G., "Ionic Liquid Ion Source Emitter Arrays Fabricated on Bulk Porous Substrates for Spacecraft Propulsion," Ph.D.Dissertation, Massachusetts Inst. of Technology, Cambridge, MA, 2011.

[25] Whittaker, C. B., and Jorns, B. A., "Statistical Characterization of Emitter Fabrication over an Electrospray Array Thruster Dataset," Deep Blue Data, Univ. of Michigan, 2024, https://deepblue.lib.umich.edu/data/concern/data_sets/6w924c77s. https://doi.org/10.7302/v8n5-a935

[26] Castro, S., and de la Mora, J. F., "Effect of Tip Curvature on Ionic Emissions from Taylor Cones of Ionic Liquids from Externally Wetted Tungsten Tips," *Journal of Applied Physics*, Vol. 105, No. 3, 2009, Paper 034903. https://doi.org/10.1063/1.3073873

[27] McGehee, W., Arnold, N., Natisin, M., Holley, Z., and Eckhardt, D., "The Single Emitter Air Force Electrospray Thruster (SEAFET) Program: Goals and Initial Results," *37th International Electric Propulsion Conference*, Electric Rocket Propulsion Soc., June 2022, p. 600, https://www.electricrocket.org/index.php?page=iepc-article-repository.

[28] Takagi, K., Tsukizaki, R., Yamshita, Y., and Takao, Y., "Effects of Tip Curvature on Multiple Emitted Ion Beams in Porous Ionic Liquid Electrospray Thrusters," *AIAA SCITECH 2024 Forum*, AIAA Paper 2024-1346, Jan. 2022. https://doi.org/10.2514/6.2024-1346

J. Rovey
Associate Editor